REPORT DOCUMENTATION PAGE

Form Approved
OMB No. 0704-0188

1. REPORT DATE *(DD-MM-YYYY)*	**2. REPORT TYPE**	**3. DATES COVERED** *(From - To)*
September 2013	Journal Article	September 2013- June 2014

4. TITLE AND SUBTITLE
Numerical Analysis of Neutral Entrainment Effect on Field Reverse

5a. CONTRACT NUMBER
In-House

5b. GRANT NUMBER

5c. PROGRAM ELEMENT NUMBER

6. AUTHOR(S)
J. Brackbill, J.-L. Cambier, N. Gimelshein, S. Gimelshein

5d. PROJECT NUMBER

5e. TASK NUMBER

5f. WORK UNIT NUMBER
QOAE

7. PERFORMING ORGANIZATION NAME(S) AND ADDRESS(ES)

Air Force Research Laboratory (AFMC)
AFRL/RQRS
1 Ara Drive.
Edwards AFB, CA, 93524-7013

8. PERFORMING ORGANIZATION REPORT NO.

9. SPONSORING / MONITORING AGENCY NAME(S) AND ADDRESS(ES)

Air Force Research Laboratory (AFMC)
AFRL/RQR
5 Pollux Dr.
Edwards AFB, CA, 93524-7048

10. SPONSOR/MONITOR'S ACRONYM(S)

11. SPONSOR/MONITOR'S REPORT NUMBER(S)
AFRL-RQ-ED-JA-2013-240

12. DISTRIBUTION / AVAILABILITY STATEMENT
Approved for public release; distribution unlimited

13. SUPPLEMENTARY NOTES
Journal article published in the Journal of Propulsion and Power, Vol. 30, Issue #6 June 2014.
PA Case Number: 13468; Clearance Date: 21 Oct 13.

14. ABSTRACT
The collisional processes between ions and electrons of a field-reversed plasmoid traveling at high speed and neutral gas particles, entrained by the plasmoid, are examined in an adiabatic bath relaxation. The importance of different reaction mechanisms, such as charge exchange, electron impact ionization, and electronic excitation with metastable atom formation and radiation, is analyzed for conditions typical for field-reversed configuration thrusters. The flow conditions include neon gas and plasma with densities on the order of 1018 molecule⁄m3, plasma temperatures between 5 and 10 eV, and relative plasma–neutral velocities up to 30 km⁄s. Then, an implicit particle-in-cell code, Celeste3D, extended to include all relevant plasma–neutral and neutral–neutral elastic and inelastic processes and Coulomb collisions, is applied to study the neutral entrainment. The model includes a planar flow between a field reversed configuration plasmoid initially at a Schmid–Burgk equilibrium and neutral gas with varying relative velocities, plasma temperatures, and neutral gas densities. The contribution of charge exchange, electron impact ionization reactions, and collisional radiation is analyzed, and the sensitivity of the entrainment efficiency to the plasmoid translation velocity and neutral density is evaluated.

15. SUBJECT TERMS

16. SECURITY CLASSIFICATION OF:			**17. LIMITATION OF ABSTRACT**	**18. NUMBER OF PAGES**	**19a. NAME OF RESPONSIBLE PERSON**
					Jean-Luc Cambier
c. REPORT	**b. ABSTRACT**	**c. THIS PAGE**	SAR	10	**19b. TELEPHONE NO** *(include area code)*
Unclassified	**Unclassified**	**Unclassified**			661-525-5655

Standard Form 298 (Rev. 8-98)
Prescribed by ANSI Std. 239.18

JOURNAL OF PROPULSION AND POWER
Vol. 30, No. 6, November–December 2014

Numerical Analysis of Neutral Entrainment Effect on Field-Reversed Configuration Thruster Efficiency

Jeremiah Brackbill,* Jean-Luc Cambier,† Natalia E. Gimelshein,* and Sergey F. Gimelshein*
ERC, Inc., Edwards Air Force Base, California 93524

DOI: 10.2514/1.B35260

The collisional processes between ions and electrons of a field-reversed plasmoid traveling at high speed and neutral gas particles, entrained by the plasmoid, are examined in an adiabatic bath relaxation. The importance of different reaction mechanisms, such as charge exchange, electron impact ionization, and electronic excitation with metastable atom formation and radiation, is analyzed for conditions typical for field-reversed configuration thrusters. The flow conditions include neon gas and plasma with densities on the order of 10^{18} molecule/m^3, plasma temperatures between 5 and 10 eV, and relative plasma–neutral velocities up to 30 km/s. Then, an implicit particle-in-cell code, Celeste3D, extended to include all relevant plasma–neutral and neutral–neutral elastic and inelastic processes and Coulomb collisions, is applied to study the neutral entrainment. The model includes a planar flow between a field-reversed configuration plasmoid initially at a Schmid–Burgk equilibrium and neutral gas with varying relative velocities, plasma temperatures, and neutral gas densities. The contribution of charge exchange, electron impact ionization reactions, and collisional radiation is analyzed, and the sensitivity of the entrainment efficiency to the plasmoid translation velocity and neutral density is evaluated.

I. Introduction

HIGH-POWER electric propulsion is one of the most promising and, at the same time, challenging propulsion technologies. The first challenge is associated with the necessity to operate a thruster at very high efficiency; otherwise, the system limitations due to heat rejection become insurmountable. It is clear that high power can be efficiently delivered into a plasma by raising its temperature, i.e., its specific energy; consequently, the specific impulse I_{sp} can take large values, even in excess of 10,000 s. However, for the fixed power available, this also translates into small thrust and acceleration. Whereas such a high I_{sp} may be highly desirable for deep space missions, the low-Earth-orbit and geosynchronous-Earth-orbit environments are mostly characterized by two competing requirements: 1) minimization of propellant and system mass (high I_{sp}), and 2) minimization of the time required for achieving the orbital maneuver (high thrust). Following the "goldilocks" principle, one must find the optimal range of I_{sp} that, depending on the mission, is usually between 2 and 5 ks. The second challenge is therefore to design an electric propulsion (EP) system that can operate in that regime at high power (50–100 kW). Finally, it is often important to operate in a dual mode, i.e., be able to switch the regime between higher thrust/lower I_{sp} and lower thrust/higher I_{sp}, at a constant power. The dual-mode operation presents the third challenge.

Plasma at high temperature inevitably becomes highly ionized, which is beneficial for coupling with external electromagnetic fields and high-efficiency thrust generation. Typical losses associated with the plasma at these conditions include radiation, effective ionization cost, and the loss of confinement. The amount of energy lost to radiation depends strongly on the conditions, but generally speaking, the line transitions are largely self-absorbed, whereas the continuum radiation is closer to being optically thin. The integrated bremsstrahlung emission (emission from decelerating electrons) is only weakly proportional to temperature, and the radiative capture rate (free-bound transitions) decreases at high temperature. Nevertheless, the rate of radiative cooling can be problematic for high-Z plasma due to a Z^2 dependence and in radiative nonequilibrium conditions (volumetric emission) [1]. The effective ionization accounts for the amount of energy required to produce an ion by electron impact, accounting for all other couplings that can reduce the electron energy; these include elastic collisions, as well as all electronic excitations, and vibrational excitations for molecular plasmas. From dependence with respect to electron energy of the cross sections for these various processes, the most efficient regime is expected for electron temperatures of the order of 50 eV. Finally, particle confinement strongly depends on applied magnetic fields, since the cross-field diffusion scales approximately [2] as $1/B$.

Due to the aforementioned factors, the optimal conditions are achieved for low-Z plasma at high (∼50 eV) temperature and in strong magnetic fields. These conditions are typically obtained in field-reversed configuration (FRC) plasma. The FRC is a self-organized magnetized plasma structure in the shape of a highly compact toroid. The magnetic field is mostly in the poloidal direction, generated by internal toroidal currents. The ratio of plasma pressure to magnetic pressure β is close to unity, i.e., the highest plasma density that can be attained for given external magnets. The poloidal field also contributes to the particle confinement. Starting from a background uniform plasma at a constant axial (bias) field, the FRC can be formed by pulsing external coils and reversing the applied field, inducing currents at the plasma boundary and "pinching" the plasma at both ends (see Fig. 1, left). The initial bias field is trapped inside the plasma and forced to reconnect at the end points (separatrix), creating an elongated toroidal shape (see Fig. 1, right).

In contrast to some other high-I_{sp} plasma propulsion concepts [3], the FRC is completely magnetically insulated from the external field; in other words, the plasma is not tied to an external field line, and the FRC can readily detach from the confining external field. It can also be translated and accelerated by applying a gradient of magnetic pressure using pulsed external coils. The FRC can therefore be efficiently accelerated to provide thrust, operates at a temperature that is optimal for ionization, and is well confined. The basic concept of operations has been demonstrated [4], and more recent research has led to further optimization of the formation process [5].

One of the latest design iterations [6] provides plasma velocities in the 10–40 km/s range: a desirable regime from the thruster efficiency standpoint. However, power and mass utilization efficiencies still remain to be determined more precisely, and thrust augmentation is still desired. Since the plasma density in the FRC is close to optimal ($\beta \approx 1$), the latter could be achieved in two ways: 1) increasing the molecular mass of the propellant; or 2) increasing the "effective" mass by gas entrainment. The first approach is by far

Received 22 November 2013; revision received 6 February 2014; accepted for publication 23 March 2014; published online 20 June 2014.

*Consultant.
†Technical Advisor, Propulsion Branch.

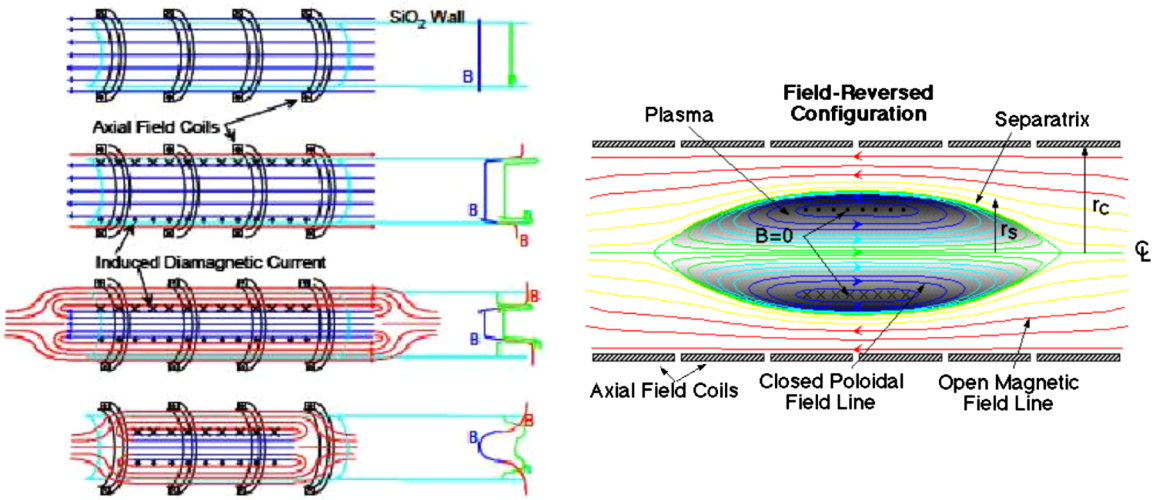

Fig. 1 Schematics of basic FRC formation by field reversal (left) and schematics of an FRC plasmoid after formation, where the crosses indicate the toroidal plasma current (right).

the easiest to achieve, and one would presume that the common propellant of choice for EP (xenon), having the largest mass of any (stable) noble gas, would be an ideal candidate. However, as previously mentioned, a high-Z plasma has higher rates of radiative and collisional (effective ionization cost) energy losses, thus reducing the efficiency. There are also some efficiency concerns discussed next.

The second approach is tentatively more attractive but more difficult to achieve. In this case, the FRC propagates into an ambient gas and entrains or pushes this neutral gas while being accelerated by the external coils. In this fashion, the system is able to exert a force on a composite object with a higher mass, whereas the plasma itself is kept at optimal physical conditions for high efficiency. The experimental proof of concept of such an entrainment has been recently presented [7]. The dynamics of the entrainment, momentum coupling, and mixing processes at the FRC/gas interface are critical to the efficiency of this concept. One of the key processes that may positively impact the entrainment efficiency is charge exchange between fast ions of the plasmoid and slow neutrals of the entrained gas. The resulting fast neutrals make significant contribution to thrust, whereas slow ions may be successively accelerated by the field. It should be noted here that the entrainment process is also key to determining the true mass utilization efficiency of the FRC thruster by itself: there is always some level of residual, ambient neutral gas in the chamber as a consequence of gas injection, whether from the previous pulse or the current one. By deliberately introducing more gas to be acted upon by the FRC formed at the end of the injection cycle, one can thus potentially improve the thrust density while remaining at peak efficiency. The numerical modeling of neutral entrainment in an FRC thruster has been considered in [7,8], where a two-fluid model was developed to take into account both neutral and plasma transports. While highly efficient from the computational standpoint, such a two-fluid model cannot capture strongly nonequilibrium velocity distributions of charged and neutral species typical for high-energy plasma–neutral interaction. A kinetic approach needs to be applied in order to properly describe such a nonequilibrium.

In this work, the process of neutral entrainment of an FRC plasmoid is studied numerically with a fully kinetic approach, with the main focus on the analysis of the relative importance of the electron impact ionization and charge exchange reactions between the neutral and charged particles. First, the balance between ionization and charge exchange reaction rates is examined for various gases and temperatures. Then, a study of heat bath relaxation is performed and the impact of Coulomb collisions is clarified. Finally, a Celeste3D particle-in-cell computational tool [9], extended to include the interactions between the charged and neutral particles and neutral particle transport, as well as Coulomb interactions between charged particles, is used in simulations of an FRC plasmoid and neutral gas interaction.

II. Reaction Rates in FRC Neutral Entrainment

There are a number of reaction processes that may play a role in the interaction of an FRC plasmoid and neutral gas, and that role depends primarily on the plasmoid density and temperature, and the translation velocity. The charge exchange reactions and the electron impact ionization are expected to be the most important processes in that interaction. Charge exchange reactions are beneficial for neutral entrainment because they produce a fast neutral particle that contributes to thrust and a slow charged particle that can be quickly and efficiently accelerated by the electromagnetic field. On the contrary, the electron impact ionization, being a highly endothermic reaction, takes away energy from the system, and therefore lowers efficiency of the thruster. Consider first xenon propellant, which appears beneficial from the propellant mass standpoint. The comparison of the reaction rates for xenon is presented in Fig. 2a. In this figure, the reaction rates for charge exchange (SCX) and ionization reactions (EII) are obtained by the integration of the corresponding cross sections

$$k_{\text{reac}} = \int g\sigma_{\text{reac}}(g) f_e(g)\,\mathrm{d}g \tag{1}$$

where g is the relative collision velocity, and f_e is the Maxwellian distribution function. Here, and in what follows, the electron impact ionization cross sections are taken from the tabulated values of the SIGLO database [10], whereas the charge exchange cross sections were assumed to have an analytic form, recommended in [11].

From recent measurements [7], one may expect the plasmoid temperature be in the range of 5 to 10 eV and the plasmoid translation velocity on the order of 20 km/s. The plasmoid translation velocity is small compared to the thermal velocity of electrons. Therefore, for electron-neutral interactions that result in ionization, the determining factor is the plasmoid temperature. For ion–neutron collisions that may result in charge exchange reactions, the kinetic energy of a 20 km/s interaction exceeds 130 eV, which corresponds to a temperature of about 65 eV, assuming a hard sphere interaction law. The comparison of ionization and charge exchange rates for xenon show that the former is expected to exceed the latter, and thus reduce the efficiency of the entrainment process. Note that, in addition to the electron impact ionization reactions, there are other mechanisms of energy loss, with most of them related to the formation of short-lived electronically excited atoms or atoms in metastable states. The reaction rate for recombination, which includes the radiative recombination in three-body collisions ($A^+ + e + e \rightarrow A + e$) and

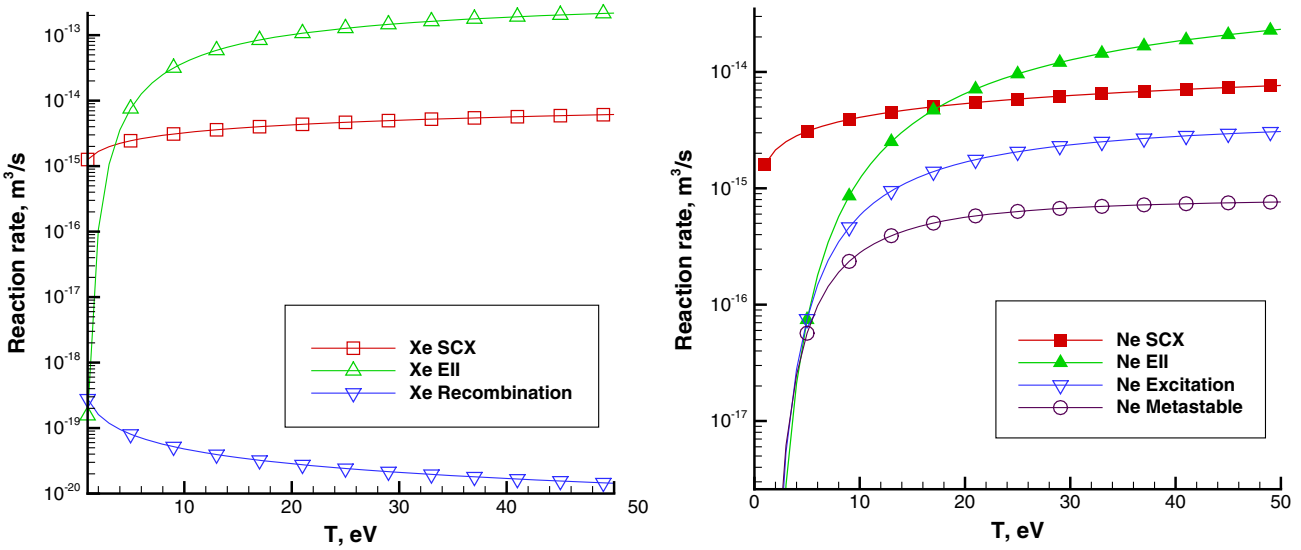

Fig. 2 Comparison of reaction rates in xenon (left) and neon (right).

the radiative photo-recombination ($A^+ + e \rightarrow A + h\nu$), is also shown in Fig. 2a. The expressions from [12] are used here. An ion and electron number density of 10^{18} m^{-3} is assumed for recombination, similar to that observed in the experiments of [4]. It is clear that the recombination cannot be a significant loss mechanism in an FRC entrainment.

Analysis of similar processes for helium (see [13], not presented here) shows that charge exchange reactions are expected to dominate for the temperature regime typical for an FRC plasmoid, primarily due to low ionization reaction rate of such light atoms. However, the small mass of helium atoms reduces the attractiveness of employing it as the main propellant. The middle ground may be found in using a gas with a larger mass that has, at the same time, a sufficiently high ionization threshold. The obvious solution here is neon, which is five times heavier than helium and has ionization energy of 21.5 eV. The comparison of ionization and charge exchange rates for neon is shown in Fig. 2b. For a plasmoid temperature of 5 eV, the charge exchange rate is over an order of magnitude higher than the electron impact excitation rate. For that temperature, there is also a noticeable amount of electron impact excitation and metastable atom formation events. The recombination reaction rate is not given here since it is much lower than the rates shown. In summary, consideration of reaction rates indicates that neon may be a promising propellant, as it is characterized by relatively small losses to radiation and ionization resulting from the interaction of charged particles of the plasmoid and neutral particles of the entrained gas. Therefore, only neon gas is examined in the following section.

III. Modeling of Collision Processes in FRC Neutral Entrainment

In the first work where kinetic modeling was used to analyze the plasmoid translation and neutral entrainment [13], the reaction processes included only the charge exchange and electron impact ionization reaction. The electronic excitation, and the resulting loss of plasmoid energy to radiation, was not considered, even though it is an important process with a rate exceeding that of the electron impact ionization at plasma temperatures of about or below 5 eV. In this work, all important relaxation and reaction processes are included in the model. Generally, the following neon states exist in neon plasma: 1) neutral atoms in the ground electronic state, 2) neutral atoms in metastable states with lifetimes in tens of seconds (effectively infinite on a sub-millisecond scale of the FRC entrainment process), 3) neutral atoms in resonant states that quickly decay into ground state (such a decay is typically fast enough to be considered instantaneous), and 4) neutral atoms in nonresonant excited states with short radiative lifetimes (14.5–27 ns) [14] (from these states, the atoms may radiatively decay either to a metastable or a resonant state), and 5) positively charged ions (only singly charged ions need to be considered in a low-Z FRC thruster environment).

Due to short lifetimes of resonant and nonresonant states as compared to the characteristic times of neutral entrainment, the excitation of ground-state atoms to resonant and nonresonant states may be regarded as the process of spontaneous photon emission, which effectively reduces the energy of the corresponding collision pair. In a kinetic modeling, therefore, only three states need to be considered, which are neutral atoms, metastable atoms, and ions. Neon has two metastable levels with closely spaced energies (16.619 and 16.716 eV), and they may be effectively lumped together without any noticeable loss of accuracy. As a result, the following processes are taken into account in this work.

1) The first process involves neon ground-state atom elastic collisions with electrons. The cross sections for high-energy elastic collisions are taken from [15,16], and the values for low-impact energies are taken from [17].

2) The second process involves elastic collisions between neutral atoms. The variable hard sphere model with parameters from [18] is applied for this interaction.

3) The third process involves Coulomb collisions between charged particles. The model [19] is implemented to compute these collisions.

4) The fourth process involves charge exchange reactions. Similar to previous work [13], the charge exchange reaction cross section of [11] is used here. The after-collision velocities of the colliding ion and neutral are swapped.

5) The fifth process involves elastic collisions between neutrals and electrons. The cross section for this process was assumed to be one-half of the charge exchange cross section, according to the recommendation of [11].

6) The sixth process involves electron impact ionization of ground-state atoms, $Ne + e \rightarrow Ne^+ + e + e$. For this reaction, the cross sections from the SIGLO database [10] are used in the computations.

7) The seventh process involves electron impact excitation of ground-state atoms to metastable states, $Ne + e \rightarrow Ne^*_M + e$. The cross sections for this process are taken from [20].

8) The eighth process involves electron impact excitation from the ground state to a short-lived excited state, followed by radiative decay into either metastable or resonance state. Since the resonance state is short-lived, and the cross section for the excitation to metastable state already takes into account the cascade contributions from higher levels; the product of this reaction should be a ground-state atom, $Ne + e \rightarrow Ne + e + h\nu$. In this work, the cross sections recommended in [21] are used.

9) The ninth process involves electron impact excitation of ground-state atoms to resonant states, followed by the radiative decay to the ground state, $Ne + e \rightarrow Ne + e + h\nu$. For this process, the cross sections are taken from [22].

10) The tenth process involves transition of metastable atoms to resonant states, with the subsequent deexcitation, $Ne_M^* + e \rightarrow Ne + e + h\nu$. The rate constant for this process is equal to $2 \cdot 10^{-7}$ cm^3/s [23], and the cross sections for kinetic modeling are calculated using the total collision energy model [24].

11) The eleventh process involves electron impact ionization of metastable atoms, $Ne_M^* + e \rightarrow Ne^+ + e + e$. The cross sections for this process are taken from [25].

12) The twelfth process involves electron impact excitation of metastable atoms to nonresonant exited states, $Ne_M^* + e \rightarrow Ne^* + e$. Since the products of this reaction are short-lived, the reaction product is a ground-state atom. The reaction cross sections follow from [21].

Processes 1–3 are elastic collisions, processes 4–5 are plasmochemical reactions, and the remaining processes define the collisional radiation model. Due to the lack of detailed, differential collision cross sections for most of the aforementioned processes, an isotropic scattering is assumed to calculate after-collision velocities of atoms and electrons in all interactions, with the exception of Coulomb collisions and charge exchange reactions.

IV. Spatially Homogeneous Relaxation of Neon Plasma

The thermal and chemical relaxation of an FRC plasmoid that collides with entrained neutral gas is a complex process that depends on a number of factors, such as plasma and neutral densities, relative collision velocities, and most importantly, the temperature of the plasmoid. Let us consider the impact of the plasmoid temperature on the time evolution of plasma and neutral properties in an adiabatic heat bath. Although the spatially homogeneous heat bath cannot accurately predict the multidimensional evolution of plasma affected by the neutral flow, it nevertheless captures the main features of the relaxation process, and thus helps in understanding the relative importance of various factors at play. To simulate the neutral entrainment process, a zero-dimensional direct simulation Monte Carlo (DSMC) code was developed that incorporates all processes listed in the previous section. It is assumed that the neutral and charged species, initially at equilibrium at their respective temperatures, have a relative velocity of 20 km/s between them; due to the symmetry of the problem, the average plasma velocity of 0 and neutral velocity of 20 km/s is assumed. The initial neutral temperature is 300 K, and the plasma temperature is either 5 or 10 eV; both neutral and plasma density are 10^{18} m^3.

The temperature profiles of neutrals T_n, ions T_i, and electrons T_e as a function of time are shown in Fig. 3 (left) for an initial plasma temperature of 5 eV. During the first few microseconds, there are not enough ionization reactions for the electron temperature to noticeably change. At the same time, the high-energy elastic collisions between neutrals and ions (their relative collision velocity of 20 km/s corresponds to an energy of 20 eV, and thus a temperature of about 10 eV) result in the increase in both ion and neutral temperatures. The maximum ion and neutral temperatures of about 9 eV are reached at about 100 μs. Note that the maximum value is impacted by the ionization and radiation losses that start to contribute after about 10 μs. The electron temperature does not have a visible maximum due to relatively slow relaxation on heavy particles, and due to energy losses to the electronic excitation/radiation and ionization. The relative contribution of the ionization and the collisional radiative processes is illustrated in Fig. 3 through the simulation of the plasma/neutral interaction with only the charge exchange and electron impact ionization included (the corresponding electron temperature is labeled "T_e no CR"). It is clear that the collisional radiation is more important for the relatively low temperature of 5 eV than the ionization processes, as it is responsible for over 70% of the electron temperature decrease. By the time of 1 ms, about 3% of the electrons and neutrals have participated in ionization.

The temperature evolution for a hotter plasma is qualitatively similar to 5 eV, but the impact of the radiation and ionization is much more pronounced in this case due to the increased rates of these processes. After 1 ms, the electron temperature decreases by almost 60%, as about 15% of electrons and neutrals participated in electron impact ionization. Most of that decrease is due to the ionization, as the corresponding temperature for the no-excitation case is about 50% of the initial temperature. Similar to the 5 eV case, the neutral and ion temperatures increase over the first 100 μs, and then they decrease due to the excitation and ionization. It is important to note that, for both initial plasma temperatures, there is a strong thermal nonequilibrium, with the species temperatures significantly different due to the elastic and inelastic collision processes.

The nonequilibrium is manifested not only at the macroscopic level with the species temperature difference but also at the microscopic level of the velocity distribution functions. The distribution functions of ion velocities in the direction of neutral–plasma relative velocity at different time moments are shown in Fig. 4 (left). Initially Maxwellian (Gaussian) distribution becomes clearly bimodal after the first few microseconds. The peak at 20 km/s corresponds to ions that participated in charge exchange reactions, and thus acquired the velocity of neutrals. The bimodality essentially disappears after about 50 μs, but the ion distribution function is still visibly non-Maxwellian even after 1 ms. The neutral atom distribution function (not shown here) is also nonequilibrium and qualitatively similar to that of ions. The nonequilibrium in the velocity distribution functions shows the importance of using a kinetic approach for modeling FRC neutral entrainment, since a continuum approximation would typically underpredict (and in some cases overpredict) the actual reaction rates.

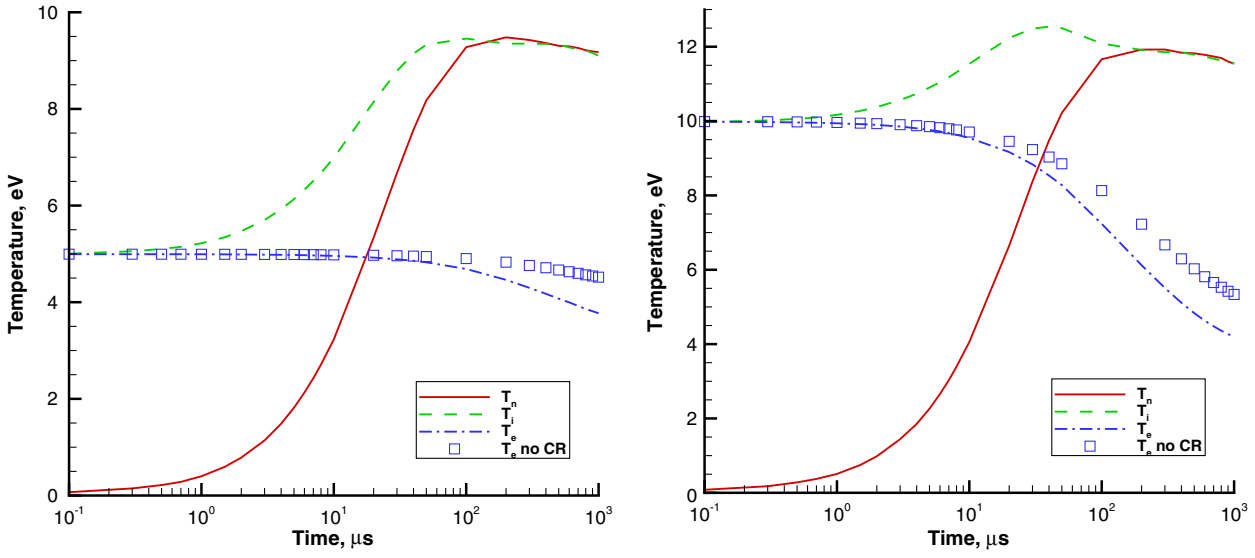

Fig. 3 Species temperature relaxation for initial plasma temperature of 5 eV (left) and 10 eV (right). CR; collisional radiation model.

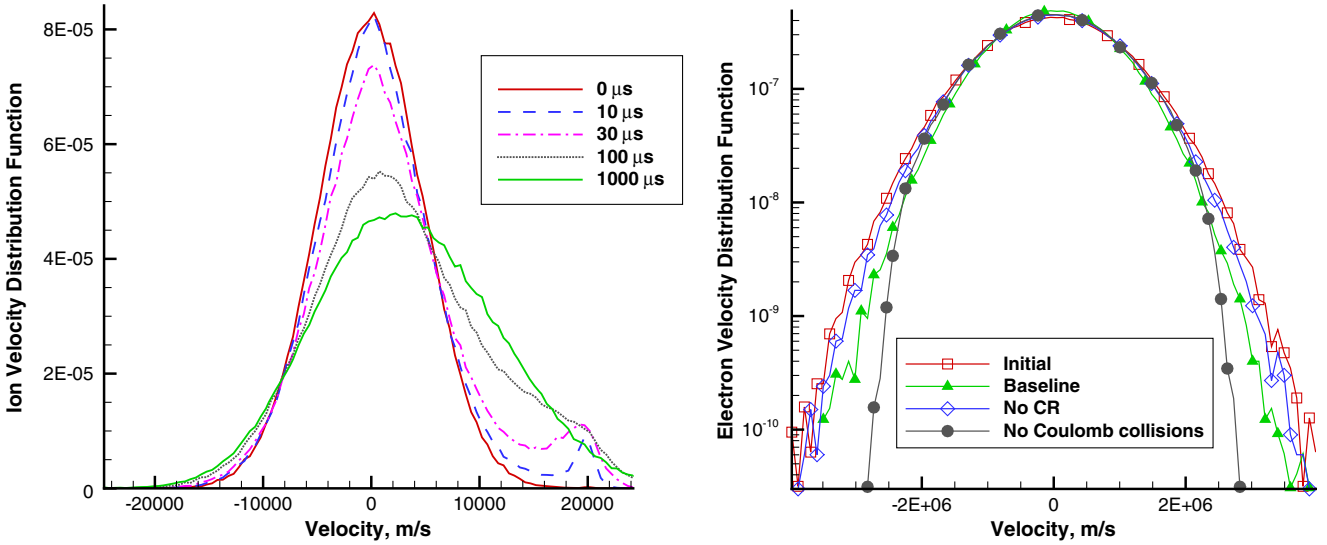

Fig. 4 Ion velocity distribution function as a function of time (left). Electron velocity distribution function at 1 ms (right). The initial plasma temperature of 5 eV.

The electron velocity distribution function is fairly close to equilibrium throughout the relaxation process, as illustrated in Fig. 4 (right) for a time moment of 1 ms. The distribution function profile is nearly Maxwellian, both for the baseline model that includes all interaction types and the model that does not take into account the excitation processes. The change in shape between the two models corresponds to the temperature difference between them discussed earlier (see Fig. 3, left). It is important to note that the principal mechanism responsible for the equilibration of the electron velocity distribution function is electron–electron Coulomb collisions. The distribution function obtained in a simulation that does not include these collisions is also presented in Fig. 4 (right); it shows a significant depletion of high-velocity tails of the distribution function. As a result, ignoring Coulomb collisions would strongly decrease the number of electronic excitations and electron impact ionizations.

V. Numerical Approach and Flow Conditions for Two-Dimensional FRC Entrainment

Although the heat bath computations presented in the previous section allow for a qualitative analysis of the outcome of neutral entrainment in terms of plasma temperature and flow non-equilibrium, and they evaluate the relative importance of different collision processes, a multidimensional simulation is required to provide some insight into the entrainment efficiency and the general thruster performance. To this end, Celeste3D is used in this work to model the process of neutral entrainment of an FRC plasmoid. Celeste3D is an implicit three-dimensional particle-in-cell (PIC) code that solves the full set of Maxwell–Vlasov equations and has been extensively used in the past for various astrophysical and laboratory plasma problems [26,27]. The implicit moment formulation of the PIC method implemented in Celeste3D results in highly efficient simulations based on ion length and timescales (and not electron scales as explicit methods do) while retaining the kinetic effects of both the electrons and the ions. An explicit simulation requires the time step to be $\Delta t < 2/\omega_{pe}$ and the spatial cell size to be $\Delta x < \zeta\lambda_e$ in order to avoid the finite grid instability. Here, ω_{pe} is the electron plasma frequency, and λ_e is the electron Debye length. In an implicit simulation, these requirements are replaced by an accuracy condition related to the conservation of energy, $\Delta t < (\Delta x/c_e)$, where c_e is the electron thermal speed.

Original Celeste3D models the evolution of ion and electron populations as described by the Vlasov equation, coupled with the solution of full Maxwell equations; it does not simulate neutral particles. To study the neutral entrainment process, Celeste3D was extended to include neutral transport and collisional relaxation. A DSMC-based capability has been added to Celeste that includes neutral transport and collisions. The included collision processes are discussed in Sec. III. As all species have different weights, a weighting scheme [28] is applied. The majorant collision frequency [29] of the DSMC method is used to model the collision process in cells.

Although the actual entrainment geometry is three-dimensional, as a nearly axisymmetric plasmoid interacts with neutral gas supplied from two or more azimuthal injectors, three-dimensional PIC modeling is extremely time consuming, and in this work, it was replaced by a two-dimensional (planar flow). The result is a much larger number of particles per cell, and thus smaller statistical scatter. The grid was 40×80, and the number of simulated ions, electrons, and neutrals per cell was approximately 64, 100, and 512, respectively. Since the cost of an implicit simulation is a direct function of the electron mass (see preceding text; the computational time is inversely proportional to the square root of the electron mass m_e), the simulation efficiency may be further enhanced through the introduction of the weighted electron mass, $m'_e = Wm_e$, where the constant $W > 1$. The ion-to-electron mass ratio has to be high enough to preserve the kinetic effects, and the value of m_i/m'_e on the order of 100 is usually sufficient [26]. In this work, $m_i/m'_e = 100$ is used (modeling of the baseline case of a 5 eV plasmoid with a neutral entrainment for a ratio of $m_i/m'_e = 300$ have shown identical results).

The initial conditions used to set an equilibrium plasmoid are given by a kinetic equilibrium in slab geometry [30,31] with an average plasma density of 10^{18} m^{-3} and two plasma temperatures of 5 and 10 eV. As explained in [32], a particle distribution function that is a function of the constants of the motion is a stationary solution of the Vlasov equation, and that is precisely what is required for a kinetic simulation. The constants of the motion in the slab geometry, the particle kinetic energy, and the particle canonical momentum in the ignored coordinate direction may be replaced by the particle kinetic energy and particle canonical angular momentum to produce an axially symmetric kinetic equilibrium [33,34]. The rigid rotor approximation discussed in [34] for axially symmetric geometries corresponds to the uniform drift approximation for slab geometries in [32] and yields similar simplifications. This could certainly be used in kinetic simulations formulated for axial symmetry but not for Celeste3D, which is formulated for three-dimensional (3-D) rectilinear grids. Compared with the magnetohydrodynamic equilibria used in fluid models, the kinetic equilibria offer less freedom to modify the pressure profile but share the same relationship between total current and plasma confinement.

To simplify the inflow boundary conditions, the neutral–plasma interaction is examined in the reference frame of the plasmoid so that

the neutral gas is injected into the computational domain from the left boundary and then passes through the domain from left to right. The properties of the injected neutral gas are changed to study their impact on the neutral–plasma interaction. In all computations, open boundary conditions for neutrals and plasma were imposed at the left and right boundaries, and a conducting wall with specular reflection was set at the top and bottom boundaries. Note that computations were also performed with no neutral inflow to analyze the temporal evolution of the plasmoid; it was observed that the equilibrium is maintained for at least 10,000 ion plasma periods. This amounts to over 30 μs for the conditions under consideration, and it is longer than the plasmoid-neutral interaction time.

VI. Modeling of FRC Entrainment

The baseline computation is conducted for the average ion and electron density inside the plasmoid of 10^{18} molecule/m^3 and plasma temperature of 5 eV, the freestream density and temperature of neutral atoms of 10^{18} molecule/m^3 and 300 K, respectively, and a relative velocity $U_{\text{rel}} = 20$ km/s between the plasmoid and neutrals. As mentioned earlier, the plasmoid–neutrals interaction is modeled in the reference frame of the plasmoid so that the plasmoid is initially not moving, and neutral gas is introduced into the computational domain with the bulk velocity of U_{rel}. Time evolution of neutral gas density is shown in Fig. 5 (left). The gas is injected from the left boundary, and the density is normalized by the freestream value. The boundary between the dark and white regions in the computational domain shows the current location of the neutral density front; the variation in density values on the order of 10% is due to statistical fluctuations related to the finite number of neutral particles per cell. After the first 0.8 μs after the beginning of the plasmoid–neutrals interaction, the neutral gas is barely visible, as it only starts flowing into the domain. At 8 μs, the neutrals advanced past the center of the computational domain into the region where the plasma density is maximum. Although there is some small decrease in neutral density due to electron impact ionization reactions, as well as some backward scattering, this effect is fairly small at this point. However, at 16 μs (the time when neutrals start to reach the outflow boundary), the effect becomes quite visible, with the loss in neutral density reaching about 20% in the central part of the flow. Again, the loss is both due to elastic and inelastic (charge exchange) interactions between neutral atoms and charged particles.

The field of the ion density normalized by 10^{18} molecule/m^3 is shown in Fig. 5 (right) at the same time moments. Note that the electron density is nearly identical, except for some statistical scatter inherent in the approach. After the first 8 μs, the impact of neutrals on the plasmoid is negligible, as the ion density is almost symmetric with respect to $X = 0.15$ m and statistically does not change as compared to the 0.8 μs case. At 16 μs, the impact of neutrals on the plasmoid is manifested through a moderate elongation of the plasmoid due to the momentum transfer between plasma and neutrals in charge exchange and elastic collisions. The increase in plasma density in the region of maximum plasma density as a result of electron impact ionization is not significant. Note that some loss of plasma particles though the outflow boundary at the right side is observed at 16 μs, The computations also showed that the electron temperature (not presented here) does not significantly change during the considered entrainment time of 16 μs; it decreases somewhat in the plasmoid region, with the total drop being close to that observed in the adiabatic heat bath (see Fig. 3).

Consider now the impact of the model and the flow conditions on the plasmoid entrainment. The results for a 5 eV plasmoid are presented in Fig. 6 (left), where the instantaneous snapshots of ion density are shown at a time of 16 μs after the neutral injection start for all cases except $U = 30$ km/s, for which it is 10.7 μs after the start of injection (this is the time that the moving neutrals need to cross the computational domain). The four cases shown are, from top to bottom, the baseline, the simulation without the collisional radiation processes, the higher neutral velocity (30 km/s instead of the baseline 20 km/s), and the elevated neutral density (5×10^{18} m^3 instead of the baseline 10^{18} m^3). All values are normalized by 10^{18}.

The comparison shows that the impact of the collisional radiation is visible but not dominant. As can be expected, the consideration of the radiation decreases the number of electron impact ionization reactions through the effective cooling of high-energy electrons. In the central region of the plasmoid, the ion density for the baseline model is only a few percent lower than for the no-radiation model. When comparing the baseline model with the case of higher relative velocity, $U = 30$ km/s, one needs to remember that the change in velocity affects two counteracting factors that impact the results. The first is the number of charge exchange reactions: a higher velocity results in a higher reaction rate, which in turn causes a translation of ions in the direction of the neutrals (and the decrease of the maximum ion density in the center of the plasmoid). The second factor is the interaction time: the higher relative velocity reduces the interaction time, and thus decreases the impact of the neutral–ion collision and reaction processes. As seen in Fig. 6 (left), the result of the velocity increase for the 5 eV case is a more compact plasmoid with a higher ion density in the central region.

The increase in the density of neutral atoms has the most pronounced effect on the plasma density field. The higher neutral density increases the likelihood of all collisional processes, and thus strongly increases the effectiveness of the neutral entrainment. The charge exchange and elastic collisions between the neutral atoms and ions result in the neutral-to-charged momentum transfer, which is manifested in the plasmoid elongation. The positive effect of the momentum transfer and the trapping of neutrals by the plasmoid is somewhat offset by the increase of the number of the electron impact ionization reactions (the number of ionization reactions increases by about a factor of three when the neutral density increases by a factor of five). The ionization reactions obviously result in the increase of the total number of charged particles, which may be beneficial for

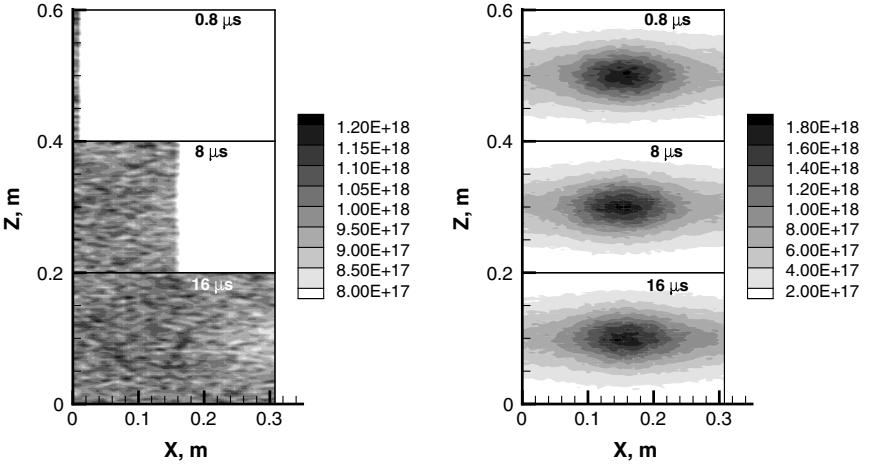

Fig. 5 Normalized neutral (left) and ion (right) number densities at different times for the baseline configuration.

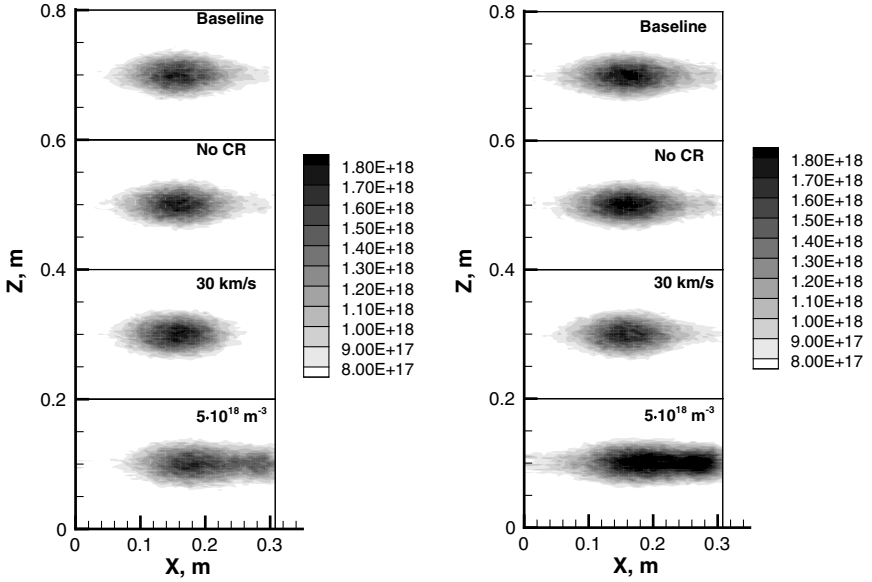

Fig. 6 Ion density for 5 eV (left) and 10 eV (right) plasma at 16 μs.

thrust production, but they also take the energy away from the plasma, which may degrade the efficiency of an FRC thruster.

The results of a similar parametric study of the 10 eV plasma case are shown in Fig. 6 (right). The radiation reaction impact is qualitatively similar to the 5 eV plasma case, although the decrease in the ion number density due to the consideration of the electronic excitation and radiation is only about 1 to 2%, and it is visible only in the center of the plasmoid. The increase in the neutral–plasma relative velocity is different for 10 eV, as it decreases the ion density in the center. The primary reason for this is that the shorter plasma–neutral interaction time becomes the primary factor in this case. Similar to the 5 eV case, the largest change in the plasmoid properties occurs when a higher neutral density of 5×10^{18} is considered. The effect is even more pronounced than for a 5 eV plasma.

VII. Thruster Efficiency Estimates

Consider now the impact of various factors and the contribution of different gas species to the thrust force produced by an FRC plasmoid. The force calculated in this work was obtained by an integration over a cross section that moves with a velocity equal to that of the neutral gas. An axial symmetry around the lower boundary is assumed in the integration in order to provide the link between the computed force and the real FRC thruster. The contribution of different components of the gas and plasma into the thruster force at different time moments is presented in Fig. 7 for the baseline case. In this figure, p denotes the contribution of the pressure component (thermal motion of particles) of the corresponding species, and ρU^2 denotes the contribution of the momentum component (translational motion). The momentum component of the electrons is negligible and not plotted here. The biggest contributor to the thrust force is the ion translational motion, which provides up to 80% of thrust. The impact of neutrals is primarily due to neutral–ion collisions, and it amounts at its peak to about 10% of the thrust force.

It has to be noted here that the FRC neutral entrainment considered in this paper includes the interaction of a plasmoid, initially at Vlasov–Maxwell equilibrium, with moving neutral gas that is injected from a boundary with a prescribed Maxwellian velocity distribution at a given average velocity and temperature. There are several differences of the considered setup from an actual operating FRC thruster. First, the reference frame of the plasmoid is chosen in the computations. Second, the numerical simulation is two-dimensional. Third, and probably most important, the modeling lacks an accelerating magnetic field. Such a field would transfer momentum to the plasmoid and replenish the momentum loss caused by the collisions with the neutrals. As the result of the latter numerical approximation, and due to the conservation of mass, momentum, and energy in the numerical modeling, the total thrust force computed over neutral and plasma species does not change when the physical model or flow conditions are modified. The indication of the entrainment efficiency is therefore the amount of energy and momentum transferred from plasma (primarily ion) species to the neutrals. The larger the decrease in thrust force produced by the ions, the stronger the entrainment.

The flow cases considered in the previous section are examined in terms of the entrainment efficiency, and the results are illustrated in Fig. 8, where the sum of thermal and translational contribution from ions is shown as a function of time. The results with no neutral flow entrainment are shown for reference purposes. For a 5 eV plasma (Fig. 8, left), the neutral entrainment results in an approximately 15% weaker contribution from ions than in the no-entrainment case. The higher velocity reduces the entrainment due to the shorter interaction time. The no-electronic-excitation case is fairly close to the baseline result, and it is not shown here. Higher neutral density reduces the ion contribution on average by a factor of two. It is interesting to note that the results for a higher initial plasma temperature of 10 eV [Fig. 8 (right)] are not just qualitatively but quantitatively similar to the 5 eV

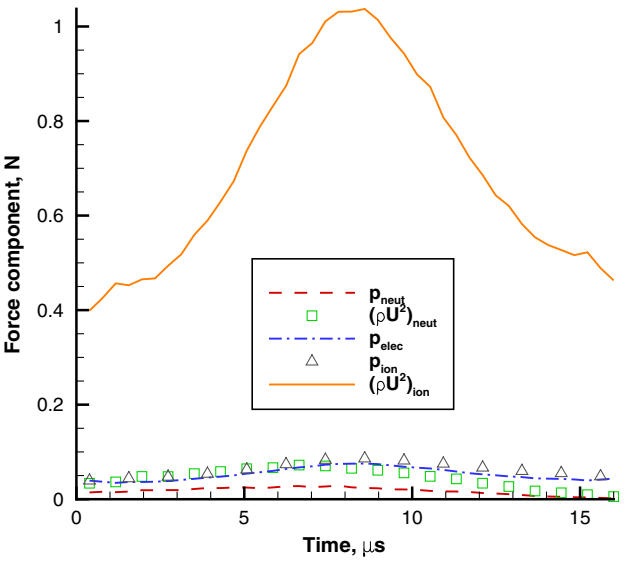

Fig. 7 Contributions of different components to the thrust force for the baseline configuration.

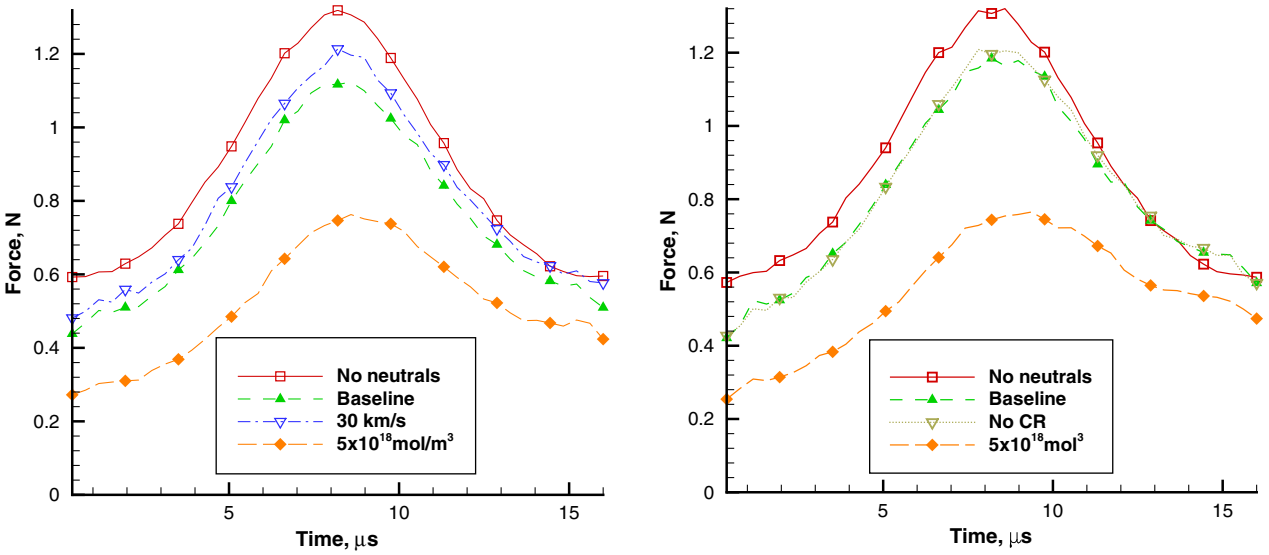

Fig. 8 Impact of various parameters on the ion contribution to the thrust force for 5 eV (left) and 10 eV (right) plasma.

cases. That indicates that the entrainment efficiency may be a weak function of temperature for temperatures in the 5 to 10 eV range.

VIII. Conclusions

This work is the first attempt to use accurate modeling at the kinetic level for analysis of a neutral entrainment in a field-reversed configuration thruster. A number of chemical and physical processes relevant for a high-speed interaction between the plasmoid and neutral gas are considered. The most important of those are charge exchange and electron impact ionization reactions and collisional processes associated with electronic excitation and radiation of neutral atoms. Analysis of chemical reaction and excitation rates presented here indicates that the use of neon as the propellant gas may be beneficial as compared to xenon due to favorable charge exchange reaction rates, and as compared to helium due to mass. Neon was therefore chosen in all simulations as a plausible propellant option.

The numerical modeling included spatially uniform thermo-chemical relaxation (adiabatic heat bath) with neutral and plasma properties close to those of a typical FRC thruster, and a two-dimensional interaction of a 5 to 10 eV FRC plasmoid, initially at a Schmid–Burgk equilibrium with an average plasma density of 10^{18} molecule/m^3, and neutral gas with comparable density. The heat bath computations showed that the relaxation process proceeds under conditions of strong thermal and chemical nonequilibrium; ion, electron, and neutral temperatures strongly differ, and the ion and neutral gas distribution function was strongly non-Maxwellian. The electron velocity distribution function was close to Maxwellian when the Coulomb collisions were taken into consideration; otherwise, electron impact ionization was found to deplete high-velocity tail of the electron distribution function. Electronic excitation and radiation processes were found to noticeably decrease primarily electron temperature, and the change was especially noticeable for interaction times exceeding 10 μs.

Two-dimensional modeling of a FRC plasmoid–neutral gas interaction is conducted with an implicit PIC code Celeste3D, extended in this work to include neutral transport, plasma–neutral, and neutral–neutral collisions and reactions and Coulomb collisions. For both 5 and 10 eV plasmoids, the results show strong entrainment of neutral particles by a translated plasmoid as a result of charge exchange reactions between slow neutrals and fast-moving ions, and a modest increase in plasma density due to electron impact ionization. The collisional radiation is found to weakly affect the entrainment process. The increase of relative velocity between the plasmoid and the neutral gas does not have a significant effect on the entrainment efficiency either. The biggest factor is the neutral gas density; a five times higher neutral density was found to reduce the ion contribution to the thrust force on average by a factor of two.

Acknowledgments

The work was supported by the U.S. Air Force Office of Scientific Research (Mitat Birkan). The authors used, in part, the Extreme Science and Engineering Discovery Environment, which is supported by National Science Foundation grant number OCI-1053575. Fruitful discussions with David Kirtley were greatly appreciated.

References

[1] McKenna, K. F., Armstrong, W. T., and Bartsch, R. R., "Particle Confinement Scaling in Field-Reversed Configurations," *Physical Review Letters*, Vol. 50, May 1983, pp. 1787–1790. doi:10.1103/PhysRevLett.50.1787

[2] Rostoker, N., and Qerushi, A., "Classical Transport in a Field Reversed Configuration," *Plasma Physics Reports*, Vol. 29, No. 7, 2003, pp. 626–630. doi:10.1134/1.1592562

[3] Elliott, F., Foster, J., and Patterson, M., "An Overview of the High Power Electric Propulsion (HiPEP) Project," AIAA Paper 2004-3453, 2004.

[4] Kirtley, D., Brown, D., and Gallimore, A., "Details on an Annular Field Reversed Configuration Plasma Device for Spacecraft Propulsion," IEPC Paper 2005-171, 2005.

[5] Miller, S., and Rovey, J., "Progress in Modeling of Pre-Ionization and Geometric Effects on a Field-Reversed Configuration Plasma Thruster," AIAA Paper 2009-3733, 2009.

[6] Slough, J., Kirtley, D., and Weber, T., "Pulsed Plasmoid Propulsion: The ELF Thruster," IEPC Paper 2009-265, 2009.

[7] Kirtley, D., Slough, J., Pihl, C., Meier, E., and Milroy, R., "Pulsed Plasmoid Propulsion: Airbreathing Electromagnetic Propulsion," IEPC Paper 2011-015, 2009.

[8] Meier, E. T., Shumlak, U., Milroy, R. D., Kirtley, D., and Slough, J., "Development and Validation of a Two-Fluid Plasma–Neutral Model," ICC Paper P2.009, Aug. 2011.

[9] Lapenta, G., and Brackbill, J., "Dynamic and Selective Control of the Number of Particles in Kinetic Plasma Simulations," *Journal of Computational Physics*, Vol. 115, No. 1, 1994, pp. 213–227. doi:10.1006/jcph.1994.1188

[10] Pitchford, L. C., Boeuf, J. P., and Morgan, W. L., "User-Friendly Boltzmann Code for Electrons in Weakly Ionized Gas," *Proceedings of the IEEE International Conference on Plasma Science*, IEEE, Piscataway, NJ, 1996.

[11] Losev, S. A., Macheret, S. O., Potapkin, B. V., and Chernyi, G. G., *Physical and Chemical Processes and Gas Dynamics: Cross Sections and Rate Constants*, Vol. 196, Progress in Astronautics and Aeronautics, AIAA, Reston, VA, 2002, pp. 71–73.

[12] Raizer, Y. P., *Gas Discharge Physics*, Springer–Verlag, Berlin, 1991, pp. 60–61.

[13] Brackbill, J., Gimelshein, S., Gimelshein, N., Cambier, J.-L., and Ketsdever, A., "Ionization and Charge Exchange Reactions in Neutral Entrainment of a Field Reversed Configuration Thruster," AIAA Paper 2012-4102, 2012.

[14] Ralchenko, Y., Kramida, A. E., and Reader, J., "NIST Atomic Spectra Database," Ver. 5, National Institute of Standards and Technology, Gaithersburg, MD, Sept. 2012, http://www.nist.gov/pml/data/asd.cfm [retrieved 2014].

[15] Brusa, R. S., Karwasz, G. P., and Zecca, A., "Analytical Partitioning of Total Cross Sections for Electron Scattering on Noble Gases," *Zeitschrift für Physik D*, Vol. 38, No. 4, 1996, pp. 279–287. doi:10.1007/s004600050092

[16] Zecca, A., Karwasz, G. P., and Brusa, R. S., "Electron Scattering by Ne, Ar and Kr at Intermediate and High Energies, 0.5–10 keV," *Journal of Physics B: Atomic and Molecular Physics*, Vol. 133, April 2000, pp. 843–845.

[17] McEachran, R. P., and Stauffer, A. D., "Electron Scattering From Neon," *Physics Letters A*, Vol. 107, No. 8, 1985, pp. 397–399. doi:10.1016/0375-9601(85)90699-1

[18] Bird, G. A., *Molecular Gas Dynamics and the Direct Simulation of Gas Flows*, Clarendon Press, Oxford, 1994, p. 458.

[19] Nanbu, K., and Yonemura, S., "Weighted Particles in Coulomb Collision Simulations Based on the Theory of a Cumulative Scattering Angle," *Journal of Computational Physics*, Vol. 145, No. 2, 1998, pp. 639–654. doi:10.1006/jcph.1998.6049

[20] Mason, N. J., and Newell, W. R., "Total Cross Sections for Metastable Excitation in the Rare Gases," *Journal of Physics B: Atomic and Molecular Physics*, Vol. 20, No. 6, 1987, pp. 1357–1378. doi:10.1088/0022-3700/20/6/020

[21] Jung, R. O., Piech, G. A., Keeler, M. L., Boffard, J. B., Anderson, L. W., and Lin, C. C., "Electron-Impact Excitation Cross Sections into Ne (2p 5 3p) Levels for Plasma Applications," *Journal of Applied Physics*, Vol. 109, No. 12, 2011, Paper 123303. doi:10.1063/1.3597826

[22] Kanik, I., Ajello, J. M., and James, J. K., "Electron-Impact-Induced Emission Cross Sections of Neon in the Extreme Ultraviolet," *Journal of Physics B: Atomic and Molecular Physics*, Vol. 29, No. 11, 1996, pp. 2355–2366. doi:10.1088/0953-4075/29/11/023

[23] Ferreira, C. M., Loureiro, J., and Ricard, A., "Populations in the Metastable and the Resonance Levels of Argon and Stepwise Ionization Effects in a Low Pressure Argon Positive Column," *Journal of Applied Physics*, Vol. 57, No. 1, 1985, pp. 82–90. doi:10.1063/1.335400

[24] Bird, G. A., "Simulation of Multi-Dimensional and Chemically Reacting Flows" *Proceedings of the 11th International Symposium on Rarefied Gas Dynamics*, edited by Campargue, R., Commissariat a l'Energie Atomique, Paris, 1979, pp. 365–388.

[25] McGuire, E., "Scaled Electron Ionization Cross Sections in the Born Approximation for Atoms with $55 < Z < 102$," *Physical Review A: General Physics*, Vol. 20, No. 2, 1979, pp. 445–456. doi:10.1103/PhysRevA.20.445

[26] Ricci, P., Lapenta, G., and Brackbill, J. U., "GEM Challenge: Implicit Kinetic Simulations with the Physical Mass Ratio," *Geophysical Research Letters*, Vol. 29, No. 23, 2002, Paper 015314. doi:10.1029/2002GL015314

[27] Lapenta, G., Brackbill, J., and Ricci, P., "Kinetic Approach to Microscopic-Macroscopic Coupling in Space and Laboratory Plasmas, in Physics of Plasmas," *Physics of Plasmas*, Vol. 13, No. 5, 2006, Paper 055904. doi:10.1063/1.2173623

[28] Gimelshein, S. F., Levin, D. A., and Collins, R. J., "Modeling of Infrared Radiation in a Space Transportation System Environment," *AIAA Journal*, Vol. 40, No. 4, 2002, pp. 781–790. doi:10.2514/2.1713

[29] Ivanov, M. S., and Rogasinsky, S. V., "Analysis of the Numerical Techniques of the Direct Simulation Monte Carlo Method in the Rarefied Gas Dynamics," *Soviet Journal of Numerical Analysis and Mathematical Modeling*, Vol. 3, No. 6, 1988, pp. 453–465.

[30] Fadeev, V. M., Kvartskhava, I. F., and Komarov, N. N., "Self-Focusing of Local Plasma Currents," *Nuclear Fusion*, Vol. 5, No. 3, 1965, pp. 202–209. doi:10.1088/0029-5515/5/3/003

[31] Schmid-Burgk, J., "Finite Amplitude Density Variations in a Self-Gravitating Isothermal Gas Layer," *Astrophysical Journal*, Vol. 149, Sept. 1967, pp. 727–729. doi:10.1086/149305

[32] Schindler, K., Pfirsch, D., and Wobig, H., "Stability of Two-Dimensional Collision-Free Plasmas," *Plasma Physics*, Vol. 15, No. 12, 1973, pp. 1163–1184. doi:10.1088/0032-1028/15/12/001

[33] Mikic, Z., and Morse, E. C., "Linear Stability Analysis of Compact Toroidal Plasmas Using Particle Simulation," *Physics of Fluids*, Vol. 30, No. 9, 1987, pp. 2806–2824.

[34] Webster, R. B., Schwarzmeier, J. L., Lewis, H. R., Choi, C. K., and Terry, W. K., "Two Dimensional Kinetic Field Reversed Equilibria," *Physics of Fluids. B, Plasma Physics*, Vol. 3, No. 4, 1991, pp. 1026–1040. doi:10.1063/1.859831

A. Gallimore
Associate Editor